Including the Temporal Dimension in the SECS Technique

S. Marsal[1], J. M. Torta[1], F. J. Pavón-Carrasco[2,3], S. P. Blake[4,5], and M. Piersanti[6]

[1]Observatori de l'Ebre (OE), Univ. Ramon Llull - CSIC, Roquetes (Spain).

[2]Universidad Complutense de Madrid (UCM), Madrid (Spain).

[3]Instituto de Geociencias (CSIC-UCM), Madrid (Spain).

[4]Department of Physics, Catholic University of America, Washington, District of Columbia, (USA).

[5]NASA Goddard Space Flight Center, Heliophysics Science Division, Greenbelt, Maryland, (USA).

[6]National Institute of Nuclear Physics, University of Rome "Tor Vergata", Rome (Italy).

Corresponding author: Santiago Marsal (smarsal@obsebre.es)

Key Points:

- The technique of Spherical Elementary Current Systems has been extended by including a temporal dependence based on cubic B-splines.
- Improvement is achieved when dealing with heterogeneous datasets consisting of geomagnetic ground data sampled at diverse rates.
- The method can be used to characterize the equivalent current systems of past and significant SW events.

Abstract

The equivalent source method of Spherical Elementary Current Systems (SECS) has contributed valuable results for spatial magnetic interpolation purposes where no observations are available, as well as for modeling equivalent currents both in the ionosphere and in the subsurface, thus providing a separation between external and internal sources. It has been successfully applied to numerous Space Weather (SW) events, whereas some advantages have been reported over other techniques such as Fourier or Spherical (Cap) Harmonic Analysis. Although different modalities of SECS exist (either 1-D, 2-D or 3-D) depending on the number of space dimensions involved, the method provides a sequence of instantaneous pictures of the source current. We present an extension of SECS consisting in the introduction of a temporal dependence in the formulation based on a cubic B-splines expansion. The technique thus adds one dimension, becoming 4-D in general (e.g., 3D + t), and its application is envisaged for, though not restricted to, the analysis of past events including heterogeneous geomagnetic datasets, such as those containing gaps, different sampling rates or diverse data sources. A synthetic model based on the Space Weather Modeling Framework (SWMF) is used to show the efficacy of the extended scheme. We apply this method to characterize the current systems of past and significant SW events producing geomagnetically induced currents (GIC), which we exemplify with an outstanding geomagnetic sudden commencement (SC) occurred on March 24, 1991.

Plain Language Summary

Spherical Elementary Current Systems (SECS) is a mathematical technique that allocates an electrical current system as the source of the geomagnetic perturbations typically recorded by ground magnetometers. Such a current system is assumed to flow on a sheet at a certain height/depth from the surface. Traditionally, SECS is a purely spatial technique, which is appropriate if we rely on homogeneous time series at each observation site. Otherwise, the information is typically concentrated at certain timestamps and sparse at others, resulting in uneven source currents being modeled. We have extended the traditional technique by including a time expansion, thus allowing spatial information to be shared across time. This produces a smoother, more realistic equivalent source current, as shown by comparing both techniques with the results of a synthetic model. We have also applied the extended method to an outstanding geomagnetic sudden commencement (SC) occurred on March 24, 1991.

1 Introduction

Spherical Elementary Current Systems (SECS) is an equivalent source method that attempts to explain the observed ground magnetic variations in terms of its current sources, which are assumed to flow on current sheets at the Earth's ionosphere and, optionally, at the subsurface. The modeling current is constructed from the superposition of a number of divergence-free elementary currents (EC), $\vec{J}_i(I_i, \vec{r})$, flowing concentrically around the knots (poles) of a predefined network (Amm, 1997; Amm & Viljanen, 1999; Marsal et al., 2017).

Knowing the ground magnetic effect of each unitary EC, $\vec{J}_i(1, \vec{r})$, and since the ground magnetic signature depends linearly on the EC intensities, the target current is obtained by inversion of the magnetic data, thus providing the EC scale factors I_i. The system to be solved is thus

$$\mathbf{B} = \mathbf{T} \cdot \mathbf{I}\,, \tag{1}$$

where **B** is the $(m \times 1)$ column matrix containing the vector components of the observed ground magnetic field at each station at time t, **I** is the $(p \times 1)$ column matrix of unknown current scale factors corresponding to each pole, and **T** is the $(m \times p)$ transfer matrix relating unitary ECs with their magnetic signature, which is constant for a given distribution of poles. Note that m is either twice the number of observatories if only the horizontal magnetic field is considered, or three times its number if the whole magnetic vector is considered, whereas p is the allocated number of poles. The system is typically solved for **I** at each time step t by use of Singular Value Decomposition (SVD). The modeled currents are generally two-dimensional; however, the name of 2D SECS is generally reserved to the case when the source current is assumed to flow in the ionosphere, whereas the technique is called 3D SECS when current sources are additionally placed in the subsurface. Once the equivalent source currents are obtained, the technique in principle allows to evaluate the ground magnetic field at any point, which is useful for *spatial* interpolation purposes (McLay & Beggan, 2010).

Since, as noted by Fukushima (1969; 1976) or Kamide et al. (1981), ground magnetic observations are basically transparent to the combination of field-aligned currents and the corresponding potential (i.e., curl-free, mainly Pedersen) currents closing in the ionosphere, only toroidal (i.e., divergence-free, mainly Hall) ionospheric currents are modeled (except for a small contribution arising from the non-radiality of field-aligned currents, which is negligible at high latitudes). The above technique thus provides equivalent (rather than real) currents. Note that this limitation can effectively be circumvented with satellite magnetic measurements, as these are sensitive to the entire system of currents. In this case, the total current is decomposed into a superposition of curl-free and divergence-free ECs, and the corresponding current scale factors are determined on the basis of the magnetic effect of both components at the satellite height. The method normally used in this context is named 1D SECS (Vanhamäki et al., 2003; Juusola et al., 2006), as the currents are assumed to vary only in one direction (usually geographical or geomagnetic latitude).

Although different modalities of SECS exist, depending on the number of space dimensions involved, the method is limited to providing a sequence of instantaneous pictures of the source currents. The extension presented in this article consists in introducing a temporal dependence in the formulation based on a cubic B-splines expansion. This type of expansion has been applied to other domains in order to determine the temporal dependence of the Gauss coefficients defining the past (e.g. Korte & Constable, 2005; Pavón-Carrasco et al., 2014) or the recent (e.g. Jackson et al., 2000; Talarn et al., 2017) secular variation of the internal Earth's magnetic field. In our case, the SECS technique becomes 4-D in general (i.e., 3-D + t). Its reliability is demonstrated in a first instance with the use of synthetic data; namely, the magnetic output of a case study obtained with the Space Weather Modeling Framework (SWMF) is used as an input for the 4D SECS method. The output of the latter is afterwards compared to the current patterns obtained with the traditional spatial version of SECS for different timestamps. In a second instance, 4D SECS has been applied to an outstanding SW event occurred on 24 March 1991, which is remarkable due to its anomalous geomagnetic sudden commencement (SC) characterized by an exceptionally large and sharp impulse in its initial part (Araki et al., 1997). The results are consistent with known upper atmospheric processes.

The range of application of the new technique is extended to cases of heterogeneous geomagnetic datasets which could hardly be treated otherwise, such as those containing gaps,

different sampling rates or diverse data sources, especially common in the past decades before the gradual standardization of the geomagnetic observations worldwide.

2 The 4D SECS method

2.1 Cubic B-splines

Basis-splines (or simply B-splines) are functions in one variable that are commonly used to fit data (e.g., De Boor, 2001). We will focus on the so-called cardinal cubic B-splines, which are written as a linear combination of basis functions b_j, each consisting of four piecewise cubic polynomials defined between five equidistant knots (except in the borders). The coefficients of the linear combination or weights, α_j, are normally determined by some modality of least squares fitting of the original data.

B-splines can be used to fit time series, such as $I(t)$, the current scale factor at each pole:

$$I(t) = \sum_{j=1}^{n} \alpha_j b_j(t) \ , \tag{2}$$

where n is the number of basis functions being used. A simple example is illustrated in Figure 1, where the blue dots denote the sampled data, and the red curve in the upper part represents the B-spline fitted curve, i.e., the superposition of the individual basis functions weighted by the corresponding coefficients, $\alpha_j b_j(t)$, appearing below. In principle, the distance between consecutive knots can be selected freely in terms of the desired time resolution of the fitted curve provided the inter-knot frequency is lower than the sampling frequency of the original data to be fitted (some restrictions to this will be discussed later).

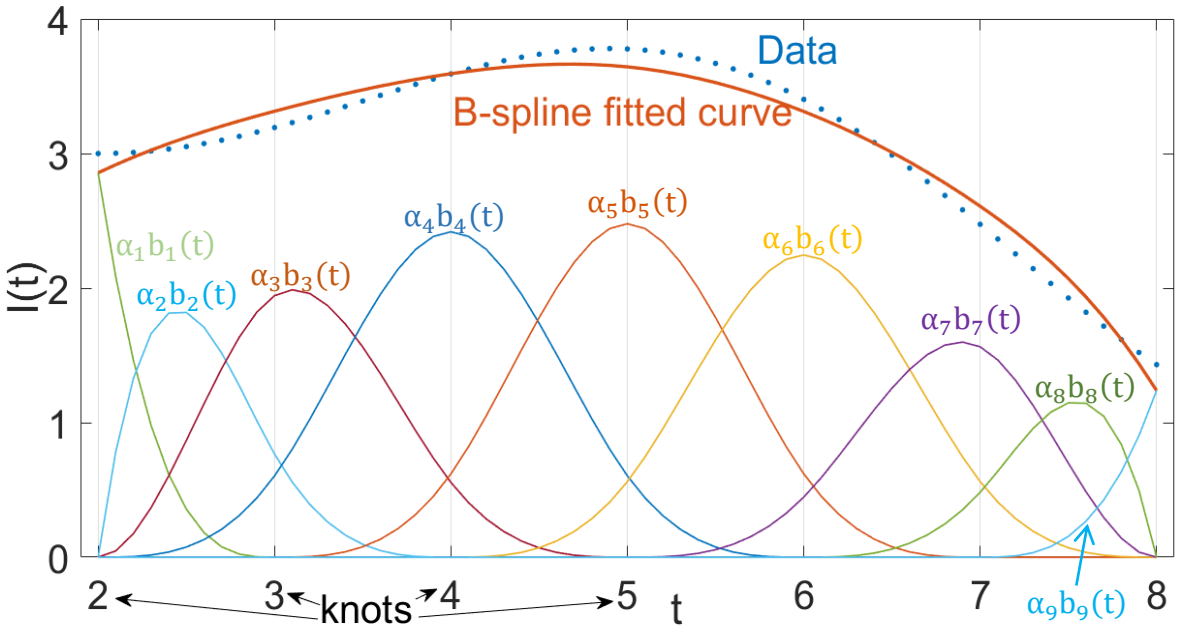

Figure 1. B-splines fitting (red curve) of an observed data series (blue dots) as a function of time. The colored curves below represent the basis functions scaled by the appropriate coefficients to adjust the data.

The basis functions b_j are determined as follows: for internal bases, continuity up to the second derivative at each knot imposes 15 equations (5 knots × 3 derivative orders) on the 16 polynomial coefficients (4 pieces × 4 coefficients/piece). We designate *peripheral* bases the three external-most bases at each end of the data interval (b_1, b_2, b_3; b_7, b_8, b_9 in Figure 1). The most external basis at each end (b_1 or b_9) simply consists of one polynomial piece between two knots (knots #2 and #3 for b_1 in the example), and is determined by imposing the above continuity conditions only on the internal knot (#3). The second basis (e.g., b_2) consists of two pieces between three knots, and is determined by imposing the above continuity conditions on the two internal knots (#3 and #4), while only continuity of the function is imposed on the external knot (#2). The third basis (e.g., b_3) consists of three pieces between four knots, and is determined by imposing the above conditions on the three internal knots (#3, #4 and #5), while only continuity up to the first derivative is imposed on the external knot (#2). Further imposing unit area of all the bases fully determines b_j.

2.2 SECS & B-splines

We can develop the elements of **I**, the matrix of current scale factors in (1), as a series of B-spline functions in the time domain, as in (2):

$$\begin{pmatrix} B_1(t) \\ \vdots \\ B_m(t) \end{pmatrix} = \begin{pmatrix} T_{11} & \cdots & T_{1p} \\ \vdots & \ddots & \vdots \\ T_{m1} & \cdots & T_{mp} \end{pmatrix} \cdot \begin{pmatrix} I_1(t) \\ \vdots \\ I_p(t) \end{pmatrix} = \begin{pmatrix} T_{11} & \cdots & T_{1p} \\ \vdots & \ddots & \vdots \\ T_{m1} & \cdots & T_{mp} \end{pmatrix} \cdot \begin{pmatrix} \sum_{j=1}^{n} \alpha_j^1 b_j(t) \\ \vdots \\ \sum_{j=1}^{n} \alpha_j^p b_j(t) \end{pmatrix}, \quad (3)$$

where the weights α_j^i of the basis functions are the unknowns. This yields:

$$\begin{pmatrix} B_1(t_1) \\ \vdots \\ B_m(t_1) \\ B_1(t_2) \\ \vdots \\ B_m(t_l) \end{pmatrix} = \begin{pmatrix} T_{11}b_1(t_1) & \cdots & T_{11}b_n(t_1) & T_{12}b_1(t_1) & \cdots & T_{1p}b_n(t_1) \\ \vdots & \ddots & \vdots & \vdots & \ddots & \vdots \\ T_{m1}b_1(t_1) & \cdots & T_{m1}b_n(t_1) & T_{m2}b_1(t_1) & \cdots & T_{mp}b_n(t_1) \\ T_{11}b_1(t_2) & \cdots & T_{11}b_n(t_2) & T_{12}b_1(t_2) & \cdots & T_{1p}b_n(t_2) \\ \vdots & \ddots & \vdots & \vdots & \ddots & \vdots \\ T_{m1}b_1(t_l) & \cdots & T_{m1}b_n(t_l) & T_{m2}b_1(t_l) & \cdots & T_{mp}b_n(t_l) \end{pmatrix} \cdot \begin{pmatrix} \alpha_1^1 \\ \vdots \\ \alpha_n^1 \\ \alpha_1^2 \\ \vdots \\ \alpha_n^p \end{pmatrix}, (4)$$

which is written in compact form as $\mathbf{B} = \mathbf{A} \cdot \boldsymbol{\alpha}$ and is solved for the $(np \times 1)$ matrix $\boldsymbol{\alpha}$. Eq. (2) then provides an analytic expression for the current scale factors as a function of time, $I_i(t)$, and therefore for the ECs, $\vec{J}_i(I_i(t), \vec{r})$, which, after superposition, give the analytic equivalent current at each level (ionosphere and/or subsurface) as a function of space and time.

The matrix **B** contains all the available information, i.e., magnetic field components at each point of space and time. Its dimensions would be $(ml \times 1)$ if there were m observations per timestamp, t_k $(k = 1, \ldots l)$; however, in general the effective number of observations at a given time is smaller than m, since not all of the magnetometers provide an observation at time t_k (either because of their reduced sampling rate or because there are gaps in the data). If we denote $m_{ef}l$ the actual length of **B**, then the new transfer matrix **A** has dimensions $(m_{ef}l \times np)$. Note

that, whereas the number of unknowns was considerably larger than the number of equations in the spatial SECS technique, now it is not necessarily the case, as the ratio unknowns/equations depends on the selected temporal resolution of the basis splines, i.e., on the ratio n/l. $\mathbf{A}$ is inverted at once by use of any suitable inversion technique, either (truncated) singular value decomposition (SVD) or regularized least squares (RLS); however, we warn that the large size of $\mathbf{A}$ may cause memory problems in some computation systems, especially when a substantial number of observation points is considered, in which case it may be necessary to reduce either the time span (l) of the data, or the splines inter-knot frequency (n).

RLS is achieved by minimizing the quantity

$$r = |\mathbf{B} - \mathbf{A} \cdot \boldsymbol{\alpha}|^2 + \lambda \boldsymbol{\alpha}^{\mathbf{T}} \cdot \boldsymbol{\phi} \cdot \boldsymbol{\alpha}\,, \tag{5}$$

where $\boldsymbol{\phi}$ is the regularization matrix and $\lambda \geq 0$ is a Lagrange multiplier which allocates the desired weight to the regularization (note that, even if least squares is used for overdetermined problems, the regularization allows a solution of the underdetermined problem, i.e., the case with more unknowns than equations). Equating to zero the partial derivatives of r with respect to $\boldsymbol{\alpha}$ and re-arranging, we get

$$\boldsymbol{\alpha} = (\mathbf{A}^{\mathbf{T}} \cdot \mathbf{A} + \lambda \boldsymbol{\phi})^{-1} \cdot \mathbf{A}^{\mathbf{T}} \cdot \mathbf{B}\,. \tag{6}$$

We have assayed different types of regularization, but one that gives results in good agreement with the traditional technique of SECS relies on the penalization of $|\boldsymbol{\alpha}|$ (and consequently of $|I(t)|$, in virtue of equation (2)), which consists of taking $\boldsymbol{\phi}$ as the $(np \times np)$ identity matrix. This has a parallelism with the method of SVD used in spatial SECS since, as noted by Amm & Viljanen (1999), the latter also minimizes $|I|$. In general, the greater the value of λ, the smoother the spatiotemporal variation of the equivalent current, but the looser adjustment of the magnetic observations. The issue of the election of λ in RLS is thus equivalent to that of the election of ε, the truncation parameter of SVD, in that a trade-off between smoothness and data fitting is to be sought.

3 Results and discussion

In order to show the strengths and weaknesses of 4D SECS, a comparison has been carried out with the spatial modality for a synthetic and a real magnetic field.

3.1 A synthetic case

In a first instance, the Space Weather Modeling Framework (SWMF) (Tóth et al., 2005) has been used to generate a synthetic though realistic magnetic input for the SECS technique.

The SWMF is an integrated framework for physics based simulations of the Sun-Earth system, from solar corona to terrestrial atmosphere (Tóth et al., 2005). It is comprised of different computational modules, each of which focuses on a different aspect of the system. In this study, the block adaptive tree solar-wind Roe-upwind scheme (BATSRUS) was used as part of the SWMF to calculate the plasma conditions in the global magnetosphere (Tóth et al., 2012), the Rice convection model was used to couple the ring current to the magnetosphere (Toffoletto et al., 2003), and the Ridley Ionospheric model was used for the ionospheric electrodynamics

(Ridley et al., 2004). A more detailed description of these modules can be found in Ngwira et al. (2014). For the simulation performed in this study, a magnetospheric grid of approximately 1 million cells was used, with a minimum cell size of 1/4 Earth radii.

In order to calculate surface magnetic field values at different locations across the globe, the Biot-Savart integral is applied to each of the current systems in the different modules that make up SWMF. These models utilize different grids and grid coordinates systems, so in order to preclude computational anomalies that may arise from transformations at the poles, no site North of 82º latitude was specified for magnetic field outputs in this study. To drive our simulation, we used solar wind conditions for the SW event which occurred on 31 March 2001. 1-minute solar wind data at 1 AU including velocity, magnetic field, density and temperature were taken from the NASA Omniweb repository (https://omniweb.gsfc.nasa.gov/). These data were linearly interpolated to 5 s temporal resolution, and small-scale synthetic noise was added to the new time-series. This random noise added at each point of the time-series was proportional to the standard deviation of a binned 2-minute window around that point.

The comparison between the spatial and 4D SECS modalities is carried out in four steps:

1- The SWMF magnetic output is calculated over time steps of 5 s on a dense virtual network of observatories homogeneously distributed over the northern hemisphere (NH). Namely, nearly 4,000 virtual observatories have been placed between geographic latitudes 0º and 82º N, which implies separations ca. 2.5º between contiguous points. The magnetic field contributed by the modeled Hall current has been used as an input to spatial 3D SECS, whose output gives the equivalent current $\vec{J}_{eq}$. The equivalent current function (ECF) ψ is afterwards calculated according to $\vec{J}_{eq} = \hat{r} \times \vec{\nabla}\psi$, which is taken as our reference.

2- The same SWMF magnetics is now calculated on the location of the real current network of observatories; namely, a total of 118 real observatories have been used over the NH (Figure 2). The ECF obtained after applying spatial SECS to the SWMF output allows assessing at what extent our *real* observatory network is capable of reproducing the *ideal* large-scale current pattern obtained in step 1.

3- Same as step 2, but instead of using a constant time step of 5 s as an input to spatial SECS, a different sampling rate has been used in each observatory in order to simulate the various cadences of magnetic recording. In practice, this consisted in removing a series of timestamps of magnetic data at certain locations (see Figure 2). The ECF has been obtained at a cadence of 5 s, i.e., the cadence corresponding to the highest sampling frequency.

4- Same as step 3, but using 4D SECS instead of spatial 3D SECS.

The results of the synthetic case have been obtained for the time interval 01:03:00 – 01:10:00 UT, 31 March 2001, corresponding to the disturbed period after the SC of the mentioned SW event. Figure 3 shows patterns of the ECF over the NH for two consecutive timestamps (01:06:00 UT, left column; 01:06:05 UT, right column) corresponding to steps 1 (upper row) through 4 (lower row). The corresponding movies for the whole 7-minute interval

can be found in the supporting material, movies S1 through S4. The left column reflects a time for which a good spatial coverage exists (all points in Figure 2), while the right one is valid for a time with a sparse coverage; namely, only observatories in North America and Japan are assumed to provide data because of its higher sampling rate (red dots only). Note that, because this is a synthetic test, the number of available observatories and corresponding sampling rates does not necessarily reflect the real situation in March 2001. Nevertheless, the depicted scenario is quite representative of the circumstances existing in the decade of 2000's.

Concerning the details of the SECS technique, we have applied the 3D modality in steps 1, 2 and 3, with the height of the ionospheric currents assumed to flow at 110 km and the subsurface currents flowing at a depth of 100 km, as in Curto et al. (2018), Marsal et al. (2017) and McLay & Beggan (2010). On the other hand, following the precepts of Amm & Viljanen (1999), the grid spacing for the poles of the ECs has been set to about one third of the average spacing between virtual (step 1) or real (steps 2, 3 and 4) observatories. This has given rise to a regular distribution of ca. 38,000 poles covering the NH in step 1. Since the distribution of real observatories is not uniform (see Figure 2), the grid of poles is irregular in steps 2, 3 and 4 (in this case, the same distribution of poles has been used as in Marsal et al., 2017, Figure 5). Concerning step 4, the interval between consecutive knots of the spline functions has been chosen to be 15 s; this figure lies between the highest and the smallest sampling rates of the magnetic observations, and determines the time resolution of the 4D SECS output. In this respect, previous knowledge of the largest frequencies of the target phenomena to be modeled may be useful, as the corresponding Nyquist frequency can be used as an upper bound for the inter-knot frequency of the spline expansion.

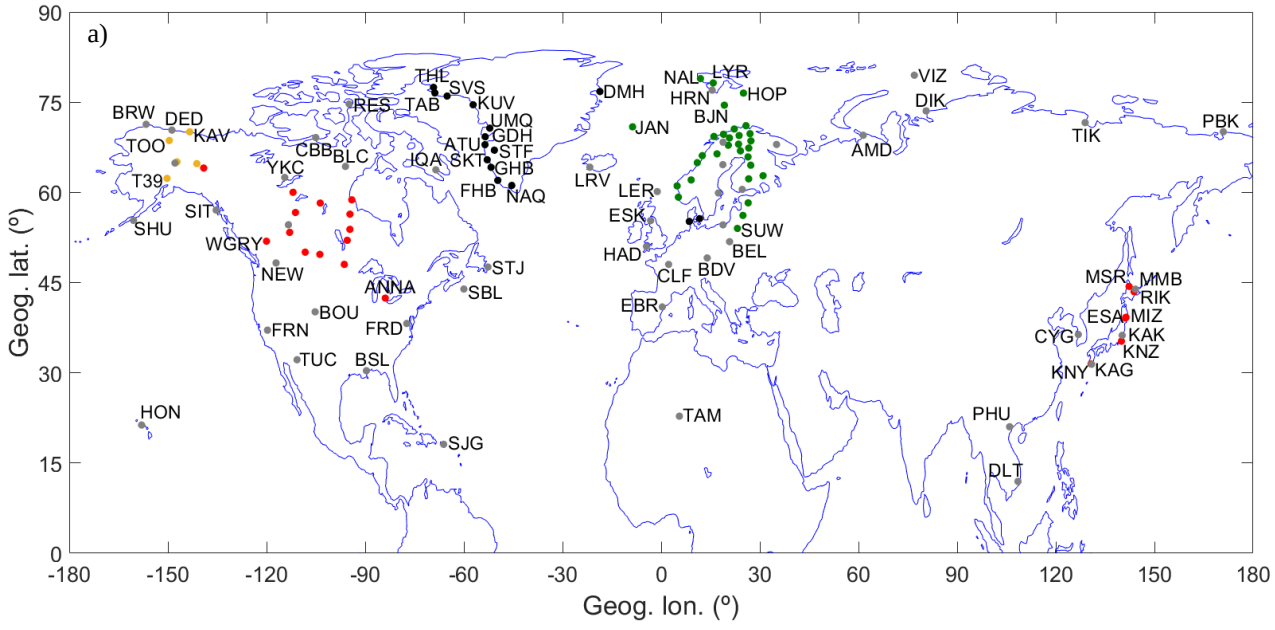

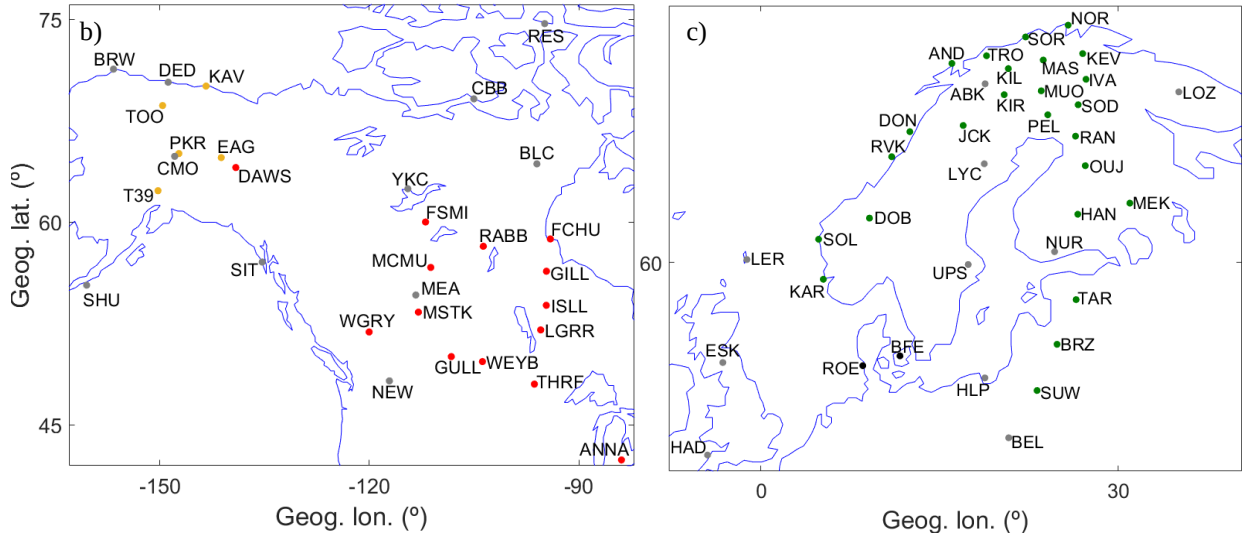

Figure 2. Location of the 118 real magnetic stations used in steps 2, 3 and 4. (**a**) NH map, (**b**) zoom on the North American sector, (**c**) zoom on the North European sector. Red, green, black, orange and grey dots denote 5 s, 10 s, 20 s, 30 s and 60 s sampling rates (steps 3 and 4), respectively.

We have used SVD to invert **A** in eq. (4). After some tests, the associated ε parameter has been chosen to be 0.02 throughout, that is, those singular values below 0.02 times the largest one have been neglected. This provides a reasonable trade-off between smoothness of the equivalent currents and data fitting. We note that, in this case, the RLS technique with a Lagrange multiplier $\lambda = 10^{-6}$ nT^{2}A^{-2} for 4D SECS gives results which are comparable to the SVD with $\varepsilon = 0.02$.

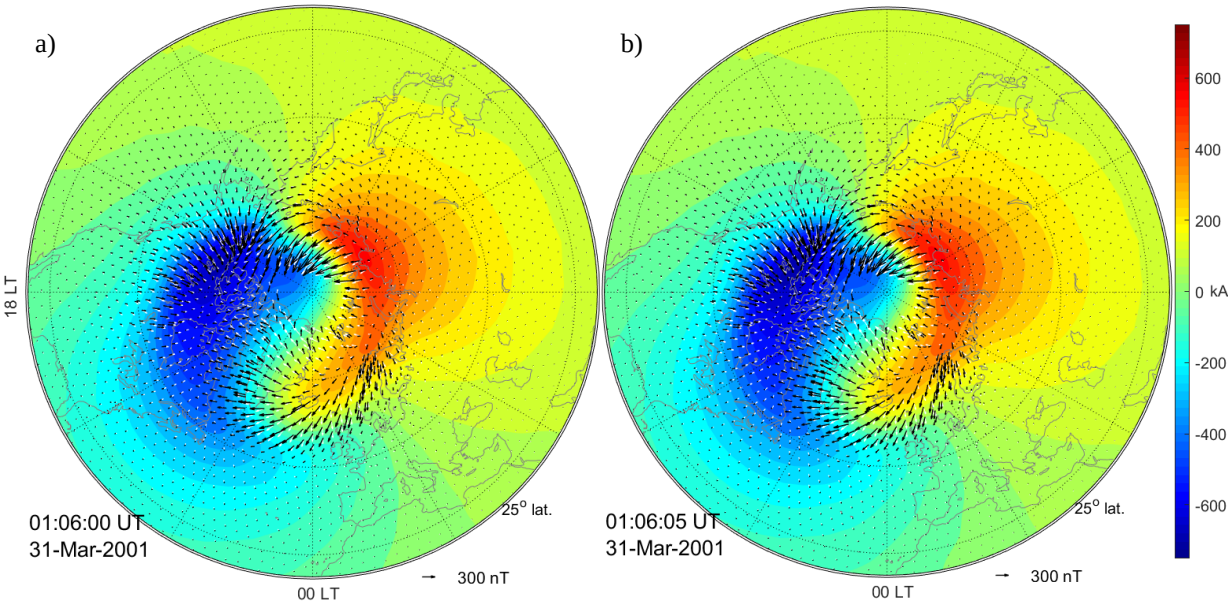

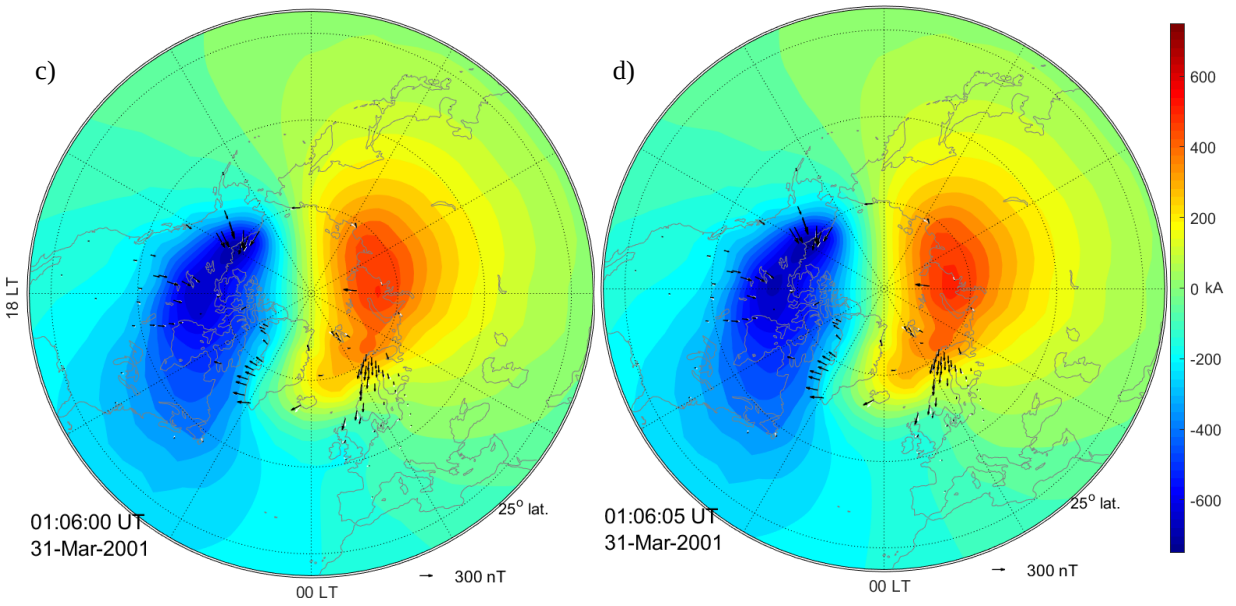
c)
d)
18 LT
01:06:00 UT
31-Mar-2001
01:06:05 UT
31-Mar-2001
25° lat.
00 LT
300 nT
600
400
200
0 kA
-200
-400
-600

272

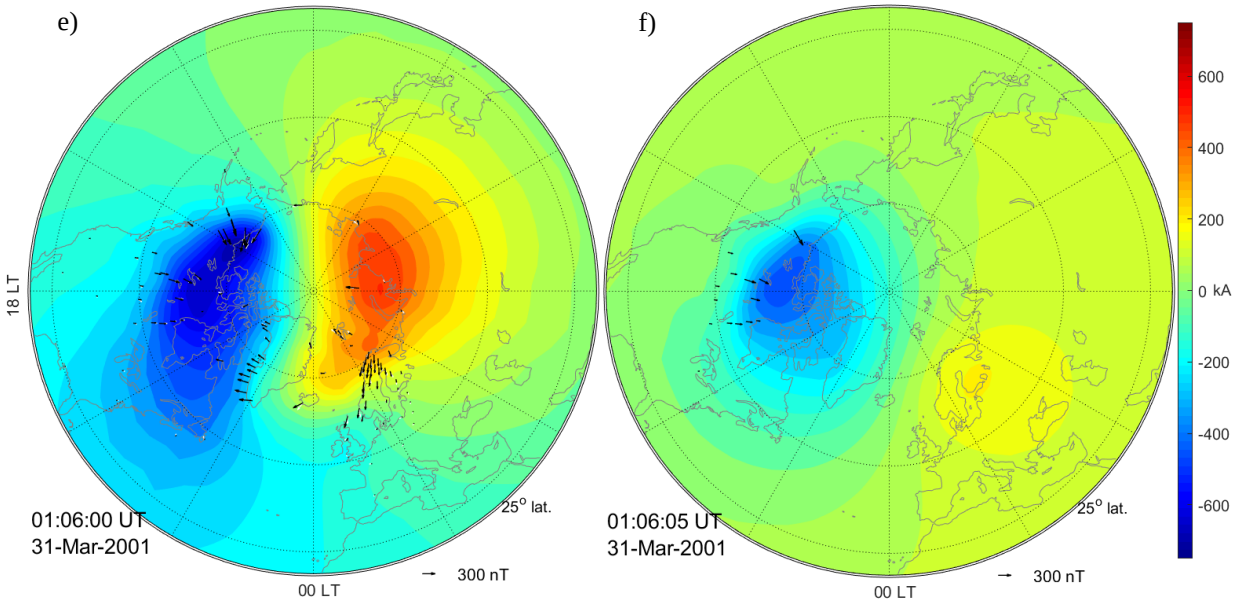
e)
f)
18 LT
01:06:00 UT
31-Mar-2001
01:06:05 UT
31-Mar-2001
25° lat.
00 LT
300 nT
600
400
200
0 kA
-200
-400
-600

273

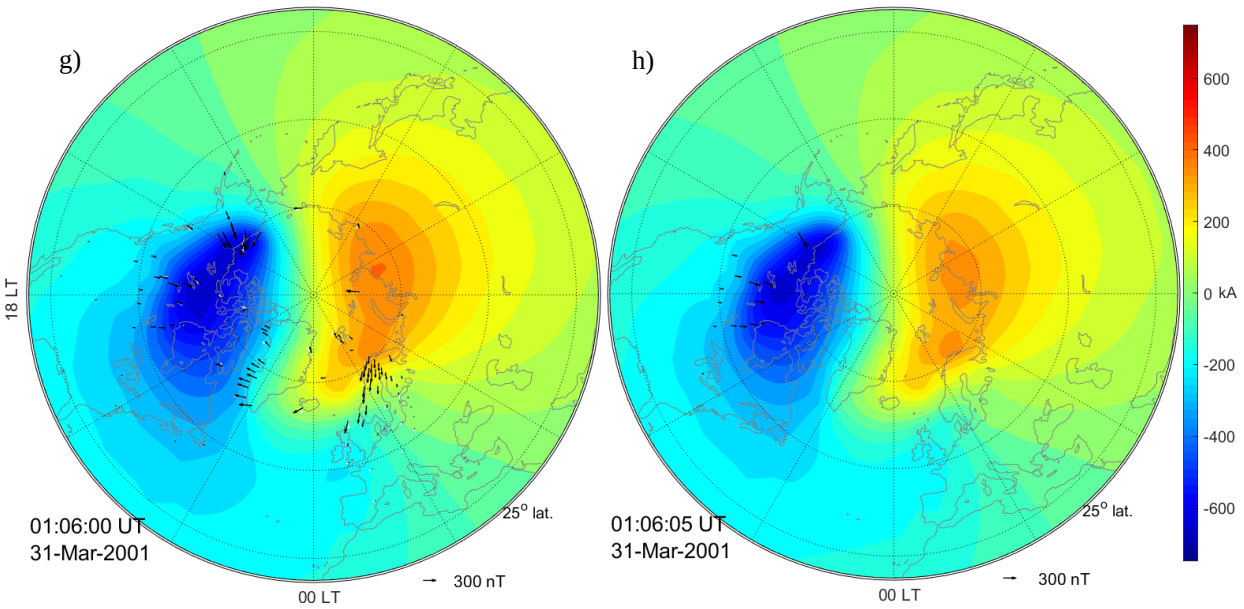

Figure 3. North Pole-centered azimuthal equidistant projection maps showing the ionospheric ECF for different simulations on the occasion of two consecutive timestamps (01:06:00, left column; 01:06:05, right column) of the post-SC phase of the March 31, 2001 SW event. A DP2 pattern can be recognized. The ECF patterns have been obtained with the SECS technique using synthetic magnetic data from the SWMF, whose simulations have been driven with solar wind data arising from the mentioned event. Panels **a** and **b** correspond to step 1 (3D SECS for high spatiotemporal density of magnetic observations); panels **c** and **d** correspond to step 2 (3D SECS for high temporal density but realistic spatial density); panels **e** and **f** correspond to step 3 (3D SECS for realistic spatiotemporal density); panels **g** and **h** correspond to step 4 (4D SECS for realistic spatiotemporal density). Black and white arrows in the observatory locations represent observed and modeled horizontal fields, respectively. Currents flow clockwise (counterclockwise) around positive (negative) patches of the ECF. The gap around the North Pole in panel **a** is aimed at preventing computational anomalies associated with the SWMF. Local noon is at the top.

3.2 Discussion of the synthetic case

A visual comparison of the first two rows of Figure 3 evidences that the realistic, irregular distribution of ground magnetometers is sufficient to reproduce the large scale pattern of the ionospheric ECF treated here (an argument that cannot be extended to smaller scales), consisting of a DP2 pattern (Disturbance of Polar origin with twin vortices). Despite this ability, differences arise where observations are scarcer, i.e., in the Siberian and the North Atlantic sectors.

In order to numerically quantify the similarity between two ECF patterns, we have used the performance parameter defined in Marsal & Torta (2019) (see also Marsal, 2015; Torta et al., 2017; Bailey et al., 2018; Ingham & Rodger, 2018; Blake et al., 2018):

$$P = 1 - \frac{RMSE_{ECFm,ECFo}}{\sigma_{ECFm}} = 1 - \sqrt{\frac{\overline{(ECF_m - ECF_o)^2}}{\overline{ECF_m}^2 - \overline{ECF_m}^2}}\,, \tag{7}$$

where ECF_m and ECF_o denote the two spatial functions to be compared at a given time, playing ECF_m the role of *model* and ECF_o the role of *objective*; $RMSE_{ECFm,ECFo}$ stands for the root mean square error between them; the bar on top a variable indicates its mean; and σ_{ECFm} represents the standard deviation of ECF_m. The RMSE is thus contextualized by the intrinsic spatial variability of the model ECF, whose role is assumed either by the pattern of step 1 or that of step 2. P is a dimensionless skill score whose maximum value is 1 for a perfect matching between both patterns and has no lower bound. Table 1 shows the values of P for different pairs of ECFs. Namely, the first two numerical rows correspond to comparisons taken at time 01:06:00 UT (i.e., concerning different patterns of the left column of Figure 3), while the last two rows correspond to comparisons taken at time 01:06:05 UT (i.e., concerning different patterns of the right column of Figure 3). For purposes of the comparison, the spatial functions ECF_m and ECF_o are defined in a geographic grid with spacing 1º latitude x 5º longitude on a spherical cap over the NH between 25º and 83º latitude.

As a proof of the above, the value of P when comparing steps 1 and 2 are found to be around 0.5 at both timestamps, reflecting a rather good resemblance. On the other hand, the ECF pattern for step 2 at 01:06:00 UT is the same as that of step 3 (panels **c** and **e** in Figure 3), as all the magnetometers provide a magnetic value at the entire minute (reason by which the corresponding entry P = 1 is obtained in Table 1). However, the differences between those same steps are noticeable at 01:06:05 UT (panels **d** and **f** in Figure 3), when only a reduced subset of the ground stations (red dots in Figure 2) provides a measurement to generate the pattern of step 3. This results in P = 0.25, which evidences a weak point of the traditional spatial SECS. In contrast, the time expansion used in 4D SECS allows the transfer of information across time, resulting in steps 2 and 4 being reasonably similar at 01:06:05 UT (panels **d** and **h**), with P rising to 0.83, whereas P decreases slightly (from 1 to 0.88) at 01:06:00 UT (panels **c** and **g**) due to the smoothing effect of the spline expansion and the ε (or λ) damping parameter.

Table 1. Skill Score P Assessing the Similarity Between Different Pairs of ECF Patterns Defined in Section 3.1. The ECF Assuming the Role of *Model* (*Objective*) is Displayed in the Header of Each Row (Column). The First (Last) Two Rows Correspond to Timestamp 01:06:00 (01:06:05) UT. Step 1: 3D SECS, High Spatiotemporal Density; Step 2: 3D SECS, Low Spatial, High Temporal Density; Step 3: 3D SECS, Low Spatiotemporal Density; Step 4: 4D SECS, Low Spatiotemporal Density.

	Step 2	Step 3	Step 4
Step 1	0.50	0.50	0.52
Step 2	-	1	0.88

Step 1	0.51	0.34	0.52
Step 2	-	0.25	0.83

3.3 A real case

For illustrative purposes, 4D SECS has been applied to an outstanding space weather event occurred on 24 March 1991, which is remarkable due to its anomalous SC characterized by an exceptionally large and sharp impulse in its initial part (Araki et al., 1997; Araki, 2014). The steep rise of geomagnetic disturbance associated with this SC produced some of the largest Geomagnetically Induced Currents (GIC) ever measured both in the United States (Kappenman, 2003) at mid-latitude locations, and in the Finnish power system (Viljanen & Pirjola, 1994).

Because we are mainly interested in the equivalent current of the ionospheric segment (mostly Hall currents), the magnetospheric contribution has been removed from the ground magnetic observations by the technique described in Piersanti & Villante (2016). In brief, the latter consists in the determination, based on the Tsyganenko & Sitnov (2005) model, of the magnetospheric current systems that mostly contribute to the observed magnetic field at a geostationary orbit. The magnetic field from such currents is then identified with the DL (Disturbance Low-latitude) field, and subtracted from the ground data according to the same model. An estimation of the contribution from field-aligned currents is also provided. After all, this technique provides the column matrix **B** in equation (4), which is solved for **α**, allowing the computation of the ionospheric equivalent or DP (Disturbance of Polar origin) current $\vec{J}_{eq}^{DP}(\vec{r},t)$.

We have used the available geomagnetic data in the NH associated with this event (see Figure 4), comprising 1 s, 5 s, 10 s, 20 s and 1-min datasets, most having multiple gaps presumably caused by saturation in the magnetic records. The inversion of matrix **A** in equation (4) has been carried out by use of SVD with $\varepsilon = 0.07$, though similar results have been obtained using RLS with $\lambda = 10^{-6.5}$ nT^{2}A^{-2}. The interval between consecutive time knots in the spline expansion has been set to 10 s in this case. Note that this is again a compromise period within the sampling rates; moreover, this interval is consistent with the frequencies reported by Araki et al. (1997), who refers to pulses of the ionospheric currents between 10 and 20 s duration for this case study.

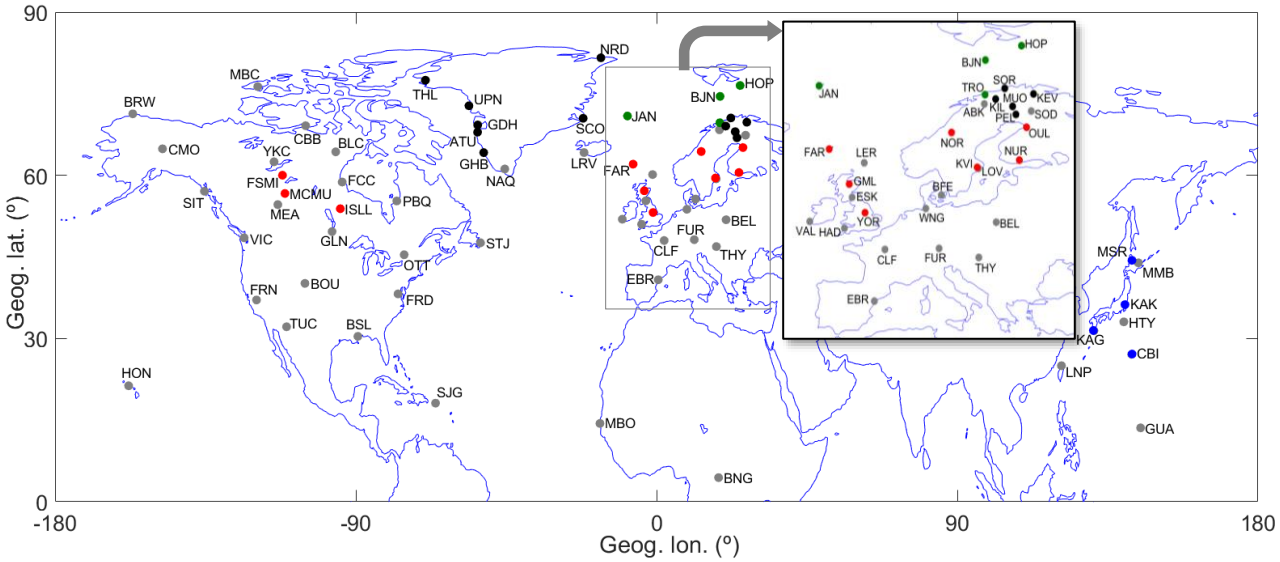

Figure 4. Location of the 73 geomagnetic stations used in the real case study. Blue, red, green, black and grey dots denote 1 s, 5 s, 10 s, 20 s, and 1-min sampling rates, respectively.

The 4D SECS technique has been run for the time interval 03:41:30 – 03:44:20 UT, and the results for some selected timestamps are presented in Figure 5. The upper panels show the NH large-scale ECF patterns, while the lower ones show smaller-scale patterns in the North-European sector. The corresponding videos are available as supporting material (movies S5 and S6). 3D SECS has also been applied for comparison purposes (movies S7 and S8).

The sparsity of ground magnetometers and the abundance of magnetic data sampled at low rates for such a fast SC event difficult a detailed analysis of the ongoing electrodynamic processes in the upper atmosphere. A comprehensive discussion of such a complex event is, besides, out of our reach; however, the 4D SECS technique allows distinguishing some recognizable ECF patterns:

1- The positive (clockwise) current vortex over North-America at 03:42:45 UT, along with the minimum in the morning sector (Figure 5, panel **a**), is consistent with a DP_{pi} (preliminary impulse) pattern. The centers of both patches are not symmetrical with respect to the noon-midnight meridian, but they are rotated counterclockwise, consistent with a compressional pulse of the solar wind in the afternoon magnetosphere. This is in line with the diagnosis made by Araki et al. (1997) and references therein (see their Figure 10), but differs in ~40 s from the first DP pulse in their Figure 9 (about 03:42:05 UT as appearing in Kakioka observatory, KAK).

2- Panel **b** is consistent with a substorm DP1 pattern (e.g., Akasofu, 2015) at 03:43:05 UT, with a strong westward current channel at nighttime auroral latitudes, though this hypothesis cannot be completely corroborated by magnetic observations in the dayside high latitudes. Note the significant extent of the equivalent currents towards mid-latitudes, whose magnetic effects are superposed to the DL field (not included here), giving rise to the intense variations recorded in ground stations.

3- Panel **c** is consistent with a westward auroral electrojet in the early morning sector during a somewhat later time of the storm initial phase (03:44:20 UT), revealing equivalent currents on the order of 1 kA/km in the peak of the channel. Panel **d** shows the contemporaneous subsurface ECF, which is opposite to the ionospheric one and somewhat weaker, as expected.

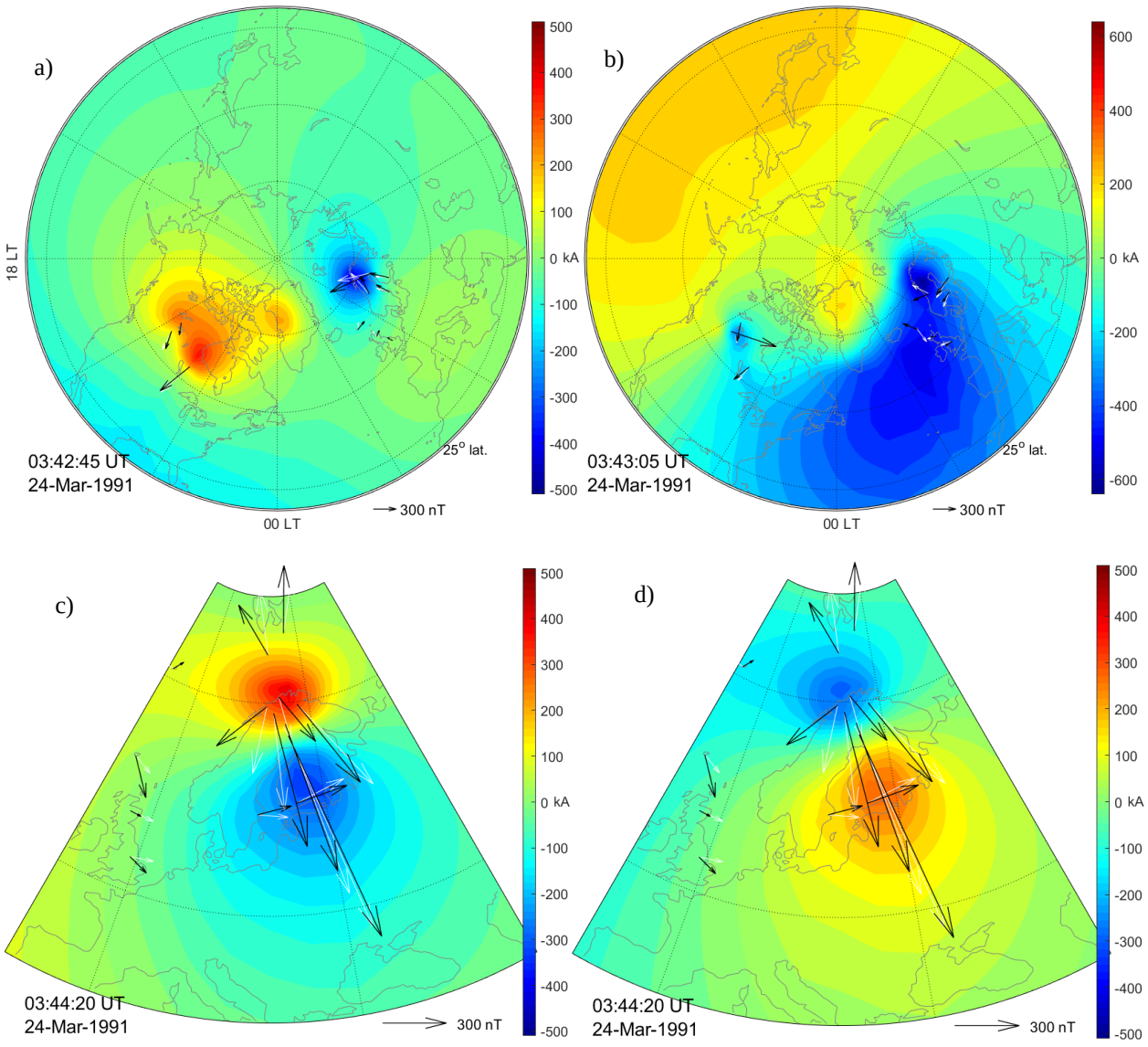

Figure 5. (**a**) Ionospheric ECF showing a DP_{pi} pattern after the SC onset of the 24 March 1991 storm, and (**b**) for a later time, where a substorm pattern (DP1) can be observed. Zoom on the European sector showing the ionospheric (**c**) and subsurface (**d**) ECF corresponding to an auroral electrojet. Black and white arrows represent observed and modeled horizontal magnetic fields, respectively. Currents flow clockwise (counterclockwise) around positive (negative) patches of the ECF. Local noon is at the top of each panel.

Figure 6 is aimed at showing an example of the performance of 4D SECS at a given location. Namely, Kakioka observatory (KAK), with 1-s records, has been selected to ease comparison with Figure 9 of Araki et al. (1997). The three panels show the different components of the magnetic field vector in the time interval 03:41:30 – 03:44:20 UT. The green line of each panel shows the field variations as they were recorded in KAK (note the arbitrary baseline); the blue line represents the field being used as an input to 4-D SECS at that particular location, which in turn corresponds to the DP field obtained from the method of Piersanti & Villante

(2016) after removal of the magnetospheric contribution; finally, the red line shows the 4-D SECS output field, i.e., the magnetic field resulting from the ECF pattern given by our method.

Firstly, some differences in strength are seen between the input DP field (blue line) and the one predicted by Araki et al. (1997) in their Figure 9, though both waveforms are similar. Differences could partly arise from the deficient coverage of satellite data in 1991, on which the method of Piersanti & Villante (2016) relies. Secondly, the input (blue) and output (red) data reasonably resemble each other, especially for the X (North) and Z (vertically downward) components. Differences arise from a) the separation between consecutive knots in the spline temporal expansion, which is tenfold the sampling period in KAK; and b) the ε damping parameter, which is necessary to avoid unreliable values outside the observation points.

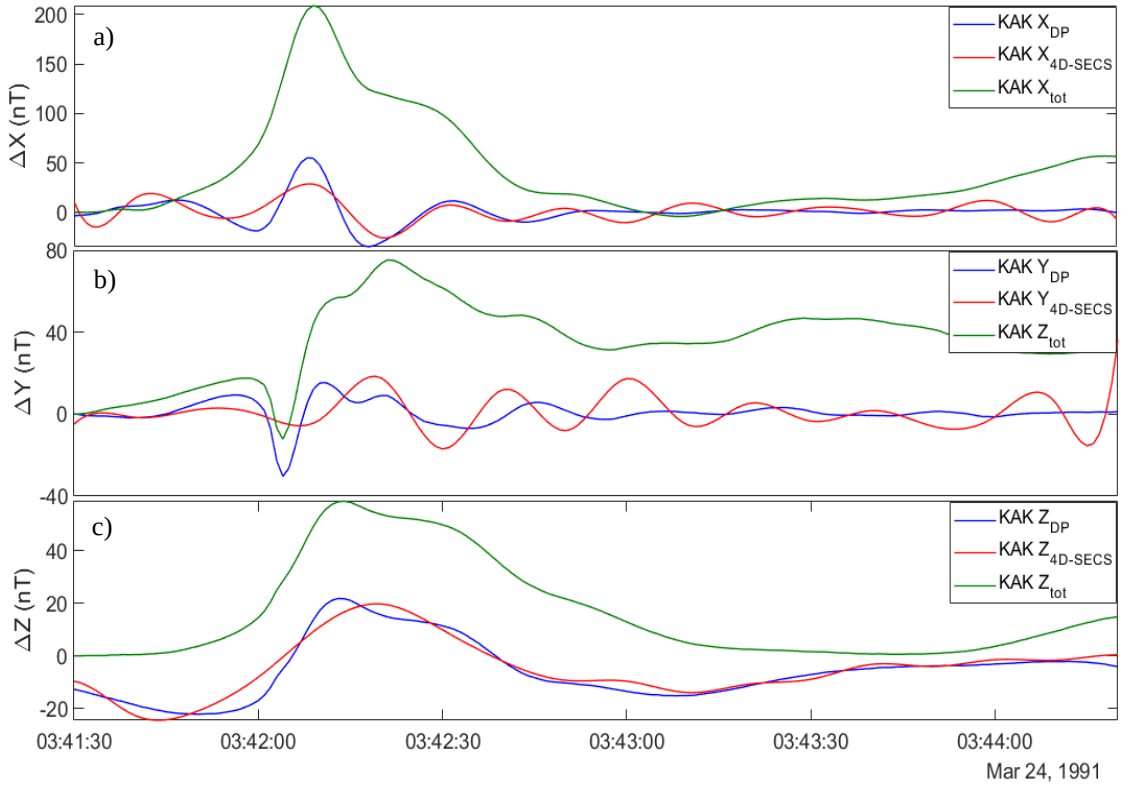

Figure 6. Magnetic field variations at Kakioka observatory (KAK) during the SC event of 24 March 1991, (**a**) North, (**b**) East, and (**c**) downward component. The green line in each panel corresponds to the recorded magnetic field; the blue line represents the DP field obtained by the method of Piersanti & Villante (2016) after removal of the magnetospheric contribution, which is used as an input to 4-D SECS; the red line is the 4D-SECS modeled magnetic field.

4 Conclusions

The temporal dimension has been included in the SECS technique by means of a spline expansion of the current scale factors that provide the spatial variation of the equivalent currents, thus converting the generally 3-D technique into 3-D + t or, shortly, 4-D. Specifically, the coefficients of the time-dependent spline basis functions are adjusted to fit the ground magnetic data spanning a pre-defined time window. This allows sharing information across the different

time frames of the referred window, thus minimizing the impact of the lack of data samples at certain observation points. Including such a time expansion into spatial SECS has been shown to confer advantages in terms of reliability and temporal continuity of the target equivalent currents to be modeled.

We emphasize that this technique is useful in cases when diverse geomagnetic sampling rates are combined, or when gaps (i.e., lack of data samples) are present in the records used as an input to SECS. Otherwise, the traditional spatial technique is recommended. A practical shortcoming of 4D SECS is its computationally expensive algorithm, a fact that may force one to either reduce the size of the time window used as an input for data inversion, or to optimize the inter-knot frequency of the spline expansion. A previous analysis of the largest expected frequencies of the phenomena under study can be useful in this context in order to avoid unnecessary knots. Problems of insufficient memory may occur nevertheless, in which case it is advisable to implement an algorithm capable of dividing the desired time window into subintervals manageable to the processor in question.

Applications of this technique include the retrospective analysis of the ionospheric sources of GIC, especially those from past and remarkable SW events, when the precepts of geomagnetic observation were far from standardized, and thus different sampling frequencies were common throughout. This has been implemented to the 24 March 1991 anomalous SC event. Although the amount of data associated with the analyzed event is scarce, the results are rather consistent with well-known SC current patterns. The modeled ionospheric currents alone are shown to be especially significant even at mid-latitudes. Another possible application of 4D SECS is the spatiotemporal interpolation of geomagnetic data, i.e., the estimation of the magnetic field vector at any point of space (provided it is surrounded by ground magnetometers), and time within the input time window.

Future lines include modeling the space-time evolution of the equivalent current flowing at the magnetopause in occasion of severe SC events, as this will help to characterize the main sources of GIC at middle and low latitudes. The use of 4D SECS to handle heterogeneous geomagnetic datasets consisting in the combination of contemporaneous data sources (such as ground and satellite measurements) is another potential field to be scrutinized.

Acknowledgments, Samples, and Data

These results are part of the project CGL2017-82169-C2-1-R “Holistic characterization of GIC in the Iberian Peninsula: from the analysis of magnetospheric and ionospheric currents to the influence of the lithosphere (IBERGIC)” funded by the Ministerio de Ciencia, Innovación y Universidades. Some of the results presented in this paper rely on data collected at magnetic observatories; we thank the national institutes that support them, INTERMAGNET for promoting high standards of magnetic observatory practice (www.intermagnet.org); the 210° MM Magnetic Observation Project (http://stdb2.stelab. nagoya-u.ac.jp/mm210/); the Canadian Array for Realtime Investigations of Magnetic Activity (CARISMA; http://www.carisma.ca/, formerly CANOPUS); the institutes who maintain the IMAGE Magnetometer Array (https://space.fmi.fi/image/www/index.php; formerly EISCAT): Tromsø Geophysical Observatory of UiT the Arctic University of Norway (Norway), Finnish Meteorological Institute (Finland), Institute of Geophysics Polish Academy of Sciences (Poland), GFZ German Research

Centre for Geosciences (Germany), Geological Survey of Sweden (Sweden), Swedish Institute of Space Physics (Sweden), and Sodankylä Geophysical Observatory of the University of Oulu (Finland); DTU Space of Denmark (http://www.space.dtu.dk/English/Research/Scientific_data_and_models/Magnetic_Ground_Stations.aspx); the Lancaster University for maintaining the SAMNET magnetometer chain; and the SUPERMAG Organization (http://supermag.jhuapl.edu/mag/?) for providing the data from the geomagnetic stations that these institutes and organizations maintain and/or provide. The original data used in this work are available from the cited institutions/websites or contact people therein. The Space Weather Modeling Framework is maintained by the University of Michigan Center for Space Environment Modeling and can be obtained at http://csem.engin.umich.edu/tools/swmf/. S.M. and J.M.T. were supported by the research project CGL2017-82169-C2-1-R; F.J.P-C is supported by the project PGC2018-099103-A-I00 of the Spanish Ministry of Science, Innovation and Universities; S.P.B's effort was supported by the NASA's Living With a Star program (17-LWS17_2-0042); M.P thanks the Italian Space Agency for the financial support under the contract ASI "LIMADOU scienza" n° 2016-16-H0v. The authors declare no conflicts of interest.

During the revision process, the relevant data used to attain the manuscript conclusions will be temporarily available at this FTP site: ftp://ftpoeb.obsebre.es/geomagnetism/4dsecs/. Once the manuscript is hypothetically accepted, these data will be deposited into an institutional repository (fulfilling FAIR policy).

References

Akasofu, S. (2015). Auroral substorms as an electrical discharge phenomenon. *Prog. in Earth and Planet. Sci., 2*, 20. https://doi.org/10.1186/s40645-015-0050-9

Amm, O. (1997). Ionospheric Elementary Current Systems in Spherical Coordinates and Their Application. *Journal of Geomagnetism and Geoelectricity*, *49*(7), 947–955. https://doi.org/10.5636/jgg.49.947

Amm, O., & Viljanen, A. (1999). Ionospheric disturbance magnetic field continuation from the ground to the ionosphere using spherical elementary current systems. *Earth, Planets and Space*, *51*, 431–440.

Araki, T, Fujitani, S., Emoto, M., Yumoto, K., Shiokawa, K., Ichinose, T., et al. (1997). Anomalous sudden commencement on March 24, 1991. *Journal of Geophysical Research: Space Physics*, *102*(A7), 14075–14086. https://doi.org/10.1029/96JA03637

Araki, Tohru. (2014). Historically largest geomagnetic sudden commencement (SC) since 1868. *Earth, Planets and Space*, *66*, 1–6. https://doi.org/10.1186/s40623-014-0164-0

Bailey, R. L., Halbedl, T. S., Schattauer, I., Achleitner, G., & Leonhardt, R. (2018). Validating GIC Models With Measurements in Austria: Evaluation of Accuracy and Sensitivity to Input Parameters. *Space Weather*, *16*(7), 887–902. https://doi.org/10.1029/2018SW001842

Blake, S. P., Gallagher, P. T., Campanyà, J., Hogg, C., Beggan, C. D., Thomson, A. W. P., et al. (2018). A Detailed Model of the Irish High Voltage Power Network for Simulating GICs.

Space Weather, 1–14. https://doi.org/10.1029/2018SW001926

Curto, J. J., Marsal, S., Blanch, E., & Altadill, D. (2018). Analysis of the solar flare effects of 6 September 2017 in the ionosphere and in the Earth's magnetic field using Spherical Elementary Current Systems. *Space Weather*, (September 2017). https://doi.org/10.1029/2018SW001927

De Boor, C. (2001). A practical Guide to Splines (Revised edition). Springer-Verlag New York Inc., United States.

Fukushima, N. (1969). Equivalence in ground magnetic effect of Chapman-Vestine's and Birkeland-Alfvén's electric current-systems for polar magnetic storms. *Rep. Ionos. Space Res. Jpn.*, *23*, 219.227.

Fukushima, N. (1976). Generalized theorem for no ground magnetic effect of vertical currents connected with Pedersen currents in the uniform conductivity ionosphere. *Rep. Ionos. Space Res. Jpn.*, *30*, 35–40.

Ingham, M., & Rodger, C. J. (2018). Telluric Field Variations as Drivers of Variations in Cathodic Protection Potential on a Natural Gas Pipeline in New Zealand. *Space Weather*, (1971), 1–14. https://doi.org/10.1029/2018SW001985

Jackson, A., Jonkers, A. R. T., Walker, M. R. (2000). Four centuries of Geomagnetic Secular Variation from Historical Records. *Philosophical Transactions of the Royal Society A: Mathematical, Physical and Engineering Sciences. 358 (1768). pp. 957–990.* http://doi.org/10.1098/rsta.2000.0569

Juusola, L., Amm, O., & Viljanen, A. (2006). One-dimensional spherical elementary current systems and their use for determining ionospheric currents from satellite measurements. *Earth, Planets and Space*, *58*, 667–678.

Kamide, Y., Richmond, A. D., & Matsushita, S. (1981). Estimation of ionospheric electric fields, ionospheric currents, and field-aligned currents from ground magnetic records. *Journal of Geophysical Research*, *86*(A2), 801. https://doi.org/10.1029/JA086iA02p00801

Kappenman, J. G. (2003). Storm sudden commencement events and the associated geomagnetically induced current risks to ground-based systems at low-latitude and midlatitude locations. *Space Weather*, 1(3), 1016, doi:10.1029/2003SW000009.

Korte, M., & Constable, C. G. (2005). Continuous geomagnetic field models for the past 7 millennia: 2. CALSK7K. *Geochem. Geophys. Geosyst.*, 6, Q02H16, doi:10.1029/2004GC000801.

Marsal, S. (2015). Conductivities consistent with Birkeland currents in the AMPERE-driven TIE-GCM. *Journal of Geophysical Research: Space Physics*, *120*(9), 8045–8065. https://doi.org/10.1002/2015JA021385

Marsal, S., & Torta, J. M. (2019). Quantifying the Performance of Geomagnetically Induced

Current Models. *Space Weather*, (2001), 941–949. https://doi.org/10.1029/2019sw002208

Marsal, S., Torta, J. M., Segarra, A., & Araki, T. (2017). Use of spherical elementary currents to map the polar current systems associated with the geomagnetic sudden commencements on 2013 and 2015 St. Patrick's Day storms. *Journal of Geophysical Research: Space Physics*, *122*(1), 194–211. https://doi.org/10.1002/2016JA023166

McLay, S. A., & Beggan, C. D. (2010). Interpolation of externally-caused magnetic fields over large sparse arrays using spherical elementary current systems. *Annales Geophysicae*, *28*, 1795–1805. https://doi.org/10.5194/angeo-28-1795-2010

Ngwira, C. M., Pulkkinen, A., Kuznetsova, M. M., & Glocer, A. (2014). Modeling extreme "Carrington-type" space weather events using three-dimensional global MHD simulations, *J. Geophys. Res.: Space Physics*, *119*, 4456-4474, doi:10.1002/2013JA019661

Pavón-Carrasco, F. J., Osete, M. L., Torta, J. M., & De Santis, A. (2014). A geomagnetic field model for the Holocene based on archaeomagnetic and lava flow data. *Earth and Planetary Science Letters*, *388*, 98–109. https://doi.org/10.1016/j.epsl.2013.11.046

Piersanti, M., & Villante, U. (2016). On the discrimination between magnetospheric and ionospheric contributions on the ground manifestation of sudden impulses. *Journal of Geophysical Research A: Space Physics*, *121*(7), 6674–6691. https://doi.org/10.1002/2015JA021666

Ridley, A. J., Gombosi, T. I., & De Zeeuw, D. L. (2004). Ionospheric control of the magnetosphere: conductance. *Annales Geophysicae*, *22*(2), 567–584. doi:10.5194/angeo-22-567-2004

Talarn, À., Pavón-Carrasco, F. J., Torta, J. M., & Catalán, M. (2017). Evaluation of using R-SCHA to simultaneously model main field and secular variation multilevel geomagnetic data for the North Atlantic. *Physics of the Earth and Planetary Interiors*, *263*. https://doi.org/10.1016/j.pepi.2016.11.008

Torta, J. M., Marcuello, A., Campanyà, J., Marsal, S., Queralt, P., & Ledo, J. (2017). Improving the modeling of geomagnetically induced currents in Spain, 691–703. https://doi.org/10.1002/2017SW001628

Toffoletto, F., Sazykin, S., & Spiro, R. Wolf, R. (2003). Inner magnetospheric modeling with the Rice Convection Model. *Space Science Reviews 107*, 175–196. https://doi.org/10.1023/A:1025532008047

Tóth, G., Sokolov, I. V., Gombosi, T. I., Chesney, D. R., Clauer, C. R., De Zeeuw, D. L., et al. (2005). Space weather modeling framework: A new tool for the space science community. *Journal of Geophysical Research: Space Physics*, *110*(A12), 1–21. https://doi.org/10.1029/2005JA011126

Tóth, G., van der Holst, B., Sokolov, I. V., De Zeeuw, D. L., Gombosi, T. I., Fang, F., Manchester, W. B., Meng, X., Najib, D., Powell, K. G., Stout, Q. F., Glocer, A., Ma, Y.-J,

585 Opher, M. (2012). Adaptive numerical algorithms in space weather modeling. *Journal of*
586 *Computational Physics*, *231*(3), 870-903. doi:10.1016/j.jcp.2011.02.006

587 Tsyganenko, N. A., & Sitnov, M. I. (2005). Modeling the dynamics of the inner magnetosphere
588 during strong geomagnetic storms. *Journal of Geophysical Research: Space Physics*, *110*,
589 1–16. https://doi.org/10.1029/2004JA010798

590 Vanhamäki, H., Amm, O., & Viljanen, A. (2003). One-dimensional upward continuation of the
591 ground magnetic field disturbance using spherical elementary current systems. *Earth,*
592 *Planets and Space*, *55*(10), 613–625. https://doi.org/10.1186/BF03352468

593 Viljanen, A. & Pirjola, R. (1994). Geomagnetically induced currents in the Finnish high-voltage
594 power system. *Surv Geophys,* 15: 383. https://doi.org/10.1007/BF00665999

595

596